

Exploring Physically-Motivated Models to Fit Gamma-Ray Burst Spectra

S. POOLAKKIL,^{1,2} R. PREECE,¹ AND P. VERES^{1,2}

¹Department of Space Science, University of Alabama in Huntsville, Huntsville, AL 35899, USA

²Center for Space Plasma and Aeronomics Research, University of Alabama in Huntsville, Huntsville, AL 35899, USA

ABSTRACT

We explore fitting gamma-ray burst spectra with three physically-motivated models, and thus revisit the viability of synchrotron radiation as the primary source of GRB prompt emission. We pick a sample of 100 bright GRBs observed by the Fermi Gamma-ray Burst Monitor (GBM), based on their energy flux values. In addition to the standard empirical spectral models used in previous GBM spectroscopy catalogs, we also consider three physically-motivated models; (a) a Thermal Synchrotron model, (b) a Band model with a High-energy Cutoff, and (c) a Smoothly Broken Power Law (SBPL) model with a Multiplicative Broken Power Law (MBPL). We then adopt the Bayesian information criterion (BIC) to compare the fits obtained and choose the best model. We find that 42% of the GRBs from the fluence spectra and 23% of GRBs from the peak-flux spectra have one of the three physically-motivated models as their preferred one. From the peak-flux spectral fits, we find that the low-energy index distributions from the empirical model fits for long GRBs peak around the synchrotron value of -2/3, while the two low-energy indices from the SBPL+MBPL fits of long GRBs peak close to the -2/3 and -3/2 values expected for a synchrotron spectrum below and above the cooling frequency.

Keywords: gamma rays: bursts — methods: data analysis

1. INTRODUCTION

The detailed nature of the radiative process responsible for gamma-ray burst (GRB) prompt emission has not yet been identified. The radiative process expected to dominate the emission is synchrotron radiation, due to the non-thermal appearance of the observed spectra and the likely presence of accelerated electrons and intense magnetic fields (Katz 1994; Rees & Meszaros 1994; Tavani 1996), but the inconsistency between the observed spectral shape at low energies and predictions from the synchrotron theory represents a challenge for this interpretation. In case of fast-cooling synchrotron radiation, the part of the spectrum immediately below the νF_ν peak energy should display a power-law behavior with a slope $\sim -3/2$, which breaks to a harder spectral shape (slope $\sim -2/3$) at lower energies (Sari et al. 1998). The prompt emission spectra of GRBs are usually fit with empirical functions, such as the Band function (Band et al. 1993), which consists of two smoothly connected power laws $N(E) \propto E^\alpha$ and $N(E) \propto E^\beta$, describing the photon spectrum at low and high energies, respectively. The typical slope of the low-energy power law is $\alpha \sim -1$ (Gruber et al. 2014; Goldstein et al. 2012). This is higher than the value expected in the case of fast-cooling synchrotron radiation.

Recent works have shown that a number of GRBs have an additional spectral break between ~ 1 and a few hundred keV (Oganesyan et al. 2017; Ravasio et al. 2019; Toffano et al. 2021) and the slopes of the power-law below and above this break are consistent with the values expected from synchrotron emission. It has been suggested that the value of α is an average value between the two power-law segments below and above the break energy. The low-energy power-law index is of particular interest for determining the emission mechanism that converts the kinetic or/and magnetic energy of the bulk relativistic outflow into radiation. Under the assumption that the emission is dominated by synchrotron radiation, the low-energy photon index should be no harder than $-3/2$ in the case of non-adiabatic cooling, and no harder than $-2/3$ in the case of adiabatic cooling (Rybicki & Lightman 1979; Katz 1994).

In this work we explore three physically-motivated models to fit GRB Spectra, and thus revisit the viability of synchrotron radiation as the source of GRB prompt emission. We pick a sample of 100 bright GRBs observed by GBM, based on their energy flux values. In addition to the empirical models used in the latest Spectral Catalog

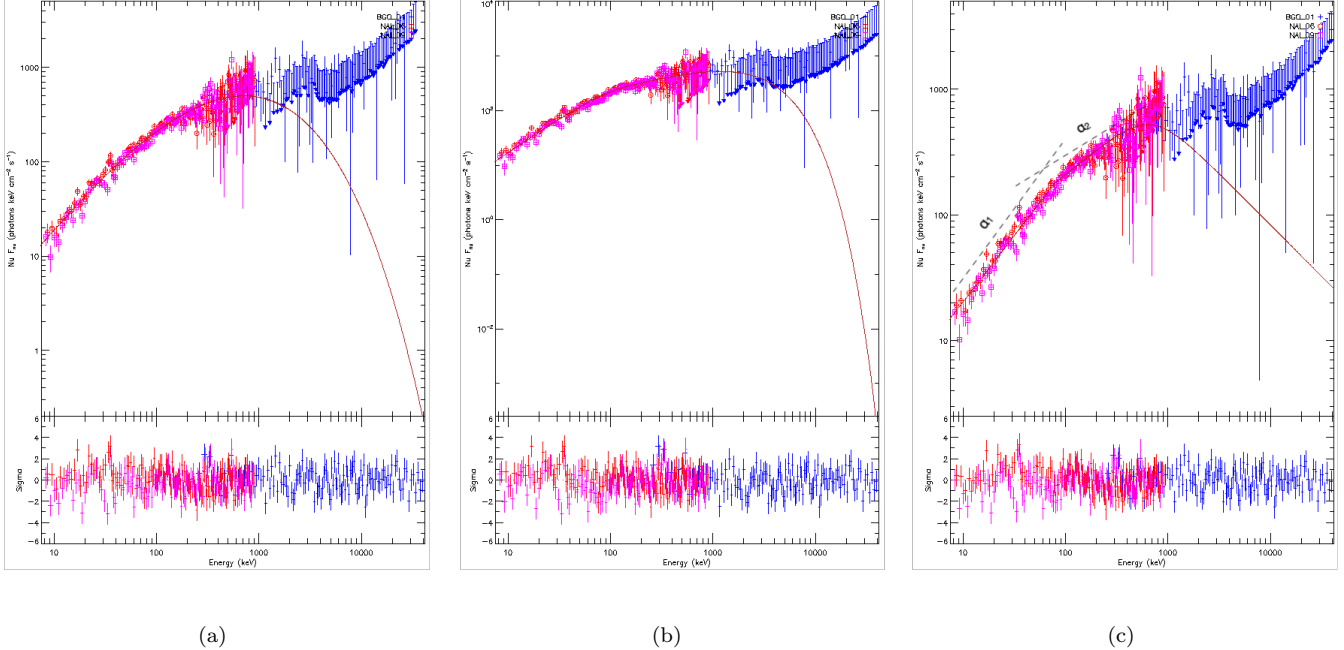


Figure 1. νF_ν (photons $\text{keV}^{-2} \text{cm}^{-2} \text{s}^{-1}$) spectrum for TS (*left*), Band+H.E. Cutoff (*middle*) and SBPL+MBPL (*right*) fits in RMfit for GRB 110921912. The pink/blue data points represent data from the NaI/BGO detectors respectively and the red dashed line represents the spectral shape predicted by the model.

(Poolakkil et al. 2021), we also consider three new models; (a) a Thermal Synchrotron model, (b) a Band model with a high-energy cutoff, with the power-law indices fixed at the synchrotron values (-0.67 and -1.5 respectively), and (c) a Smoothly Broken Power-law (SBPL) model with a multiplicative broken power-law (MBPL). We then adopt the Bayesian information criterion (Neath & Cavanaugh 2012) to compare the fits obtained and choose the best one.

2. ANALYSIS METHOD

2.1. Instrument and Sample Selection

Fermi GBM consists of 14 detector modules: 12 Sodium Iodide (NaI) detectors, covering the energies 8 - 1000 keV, and two Bismuth Germanate (BGO) detectors, covering 200 keV to 40 MeV (Meegan et al. 2009). Data selection is identical to that as described in previous spectroscopy catalogs (Gruber et al. 2014; Poolakkil et al. 2021). In brief, up to three NaI detectors with observing angles to the source less than 60° are selected, along with the BGO detector that has the smallest observing angle of the burst. For each of these, standard energy ranges that avoid unmodeled effects, such as an electronic roll-off at low energies and high-energy overflow bins are selected. Each data set is binned according to whether the burst is long (1.024 s binning) or short (0.064 s binning), with a dividing line at $T_{90} = 2$ s (Kouveliotou et al. 1993), where T_{90} is the time between the 5% and 95% values of the total fluence. Next, a background model (polynomial in time) is chosen to fit regions of the light curve that bracket the emission interval.

The analyses presented herein are comprised of two spectra for each burst: a ‘fluence’ (F) spectrum that represents the entire duration of emission and a ‘peak flux’ (P) spectrum that depicts the brightest portion of each burst, on a fixed timescale of 1.024 s for long GRBs and 64 ms for short GRBs. The selection of fluence time bins for each of these two classes is made by including every (energy-integrated) time bin that has flux that is at least 3.5 sigma in excess of the background model for that bin. The data is then joint fit with RMfit (version 4.5.3¹, available at the Fermi Science Support Center), using a set of standard model functions (Section 2.2). For a fit statistic, we have chosen the pgstat

¹ <https://fermi.gsfc.nasa.gov/ssc/data/analysis/user/>

statistic (Arnaud et al. 2011), which properly accounts for the Gaussian uncertainties in the background, arising from the temporal fit.

2.2. Models

We chose seven spectral models to fit the spectra of GRBs in our sample. In addition to the empirical spectral functions used in the latest spectroscopy catalog, we consider three additional models that are physically motivated (Bauke 2007; Arnold 2015). We also consider the COMP and BAND models with a Black Body component added to them. All models are formulated in units of photon flux with energy (E), temperature (kT) in keV and multiplied by a normalization constant A (photon s⁻¹ cm⁻² keV⁻¹). Note that for the SBPL+MBPL model, the two low-energy indices before and after the MBPL break energy will be referred to as α_1 and α_2 respectively, as highlighted in Figure 1(c). The pivot energy (E_{piv}) normalizes the model to the energy range under consideration and helps reduce cross-correlation of other parameters. In all cases, E_{piv} is held fixed at 100 keV.

- **COMP:** An exponentially-attenuated power law ('comptonized'), with normalization (A), low-energy power-law index (α) and characteristic energy (E_{peak})

$$f_{\text{COMP}}(E) = A \left(\frac{E}{E_{\text{piv}}} \right)^{\alpha} \exp \left[-\frac{(\alpha+2)E}{E_{\text{peak}}} \right] \quad (1)$$

- **BAND:** The Band GRB function, with normalization (A), low-energy power-law index (α), high-energy power-law index (β) and characteristic energy (E_{peak})

$$f_{\text{BAND}}(E) = A \begin{cases} \left(\frac{E}{100 \text{ keV}} \right)^{\alpha} \exp \left[-\frac{(\alpha+2)E}{E_{\text{peak}}} \right], & E \geq \frac{(\alpha-\beta)E_{\text{peak}}}{\alpha+2} \\ \left(\frac{E}{100 \text{ keV}} \right)^{\beta} \exp \left(\beta - \alpha \right) \left[\frac{(\alpha-\beta)E_{\text{peak}}}{100 \text{ keV}(\alpha+2)} \right]^{\alpha-\beta}, & E < \frac{(\alpha-\beta)E_{\text{peak}}}{\alpha+2} \end{cases} \quad (2)$$

- **SBPL:** A smoothly broken power law, with normalization (A), low-energy power-law index (λ_1), high-energy power-law index (λ_2), a characteristic break energy (E_b) and the break scale (Δ), in decades of energy. As in Gruber et al. (2014), we keep the value of Δ fixed at 0.3.

$$f_{\text{SBPL}}(E) = A \left(\frac{E}{E_{\text{piv}}} \right)^b 10^{(a-a_{\text{piv}})}, \quad (3)$$

where:

$$\begin{aligned} a &= m\Delta \ln \left(\frac{e^q + e^{-q}}{2} \right), & a_{\text{piv}} &= m\Delta \ln \left(\frac{e^{q_{\text{piv}}} + e^{-q_{\text{piv}}}}{2} \right), \\ q &= \frac{\log(E/E_b)}{\Delta}, & q_{\text{piv}} &= \frac{\log(E_{\text{piv}}/E_b)}{\Delta}, \\ m &= \frac{\lambda_2 - \lambda_1}{2}, & \text{and } b &= \frac{\lambda_2 + \lambda_1}{2} \end{aligned}$$

- **MBPL:** A Multiplicative Broken Power Law, which can be used as a low-energy or high-energy cutoff by fixing λ_h or λ_l at zero, respectively

$$f_{\text{MBPL}}(E) = \begin{cases} (E/E_b)^{\lambda_l}, & E \leq E_b \\ (E/E_b)^{\lambda_h}, & E > E_b \end{cases} \quad (4)$$

- **Black Body:** A Black Body spectrum with normalization (A) and temperature (kT)

$$f_{\text{BB}}(E) = A \left(\frac{E^2}{\exp(E/kT) - 1} \right) \quad (5)$$

- **High-energy Cutoff:** A multiplicative component with a cutoff energy (E_{cut}) and folding energy (E_F)

$$f_{\text{HEC}}(E) = \begin{cases} 1, & E \leq E_{\text{cut}} \\ (E/E_{\text{cut}})^{(E_{\text{cut}}/E_F)} \exp \left[\frac{(E_{\text{cut}}-E)}{E_F} \right], & E > E_{\text{cut}} \end{cases} \quad (6)$$

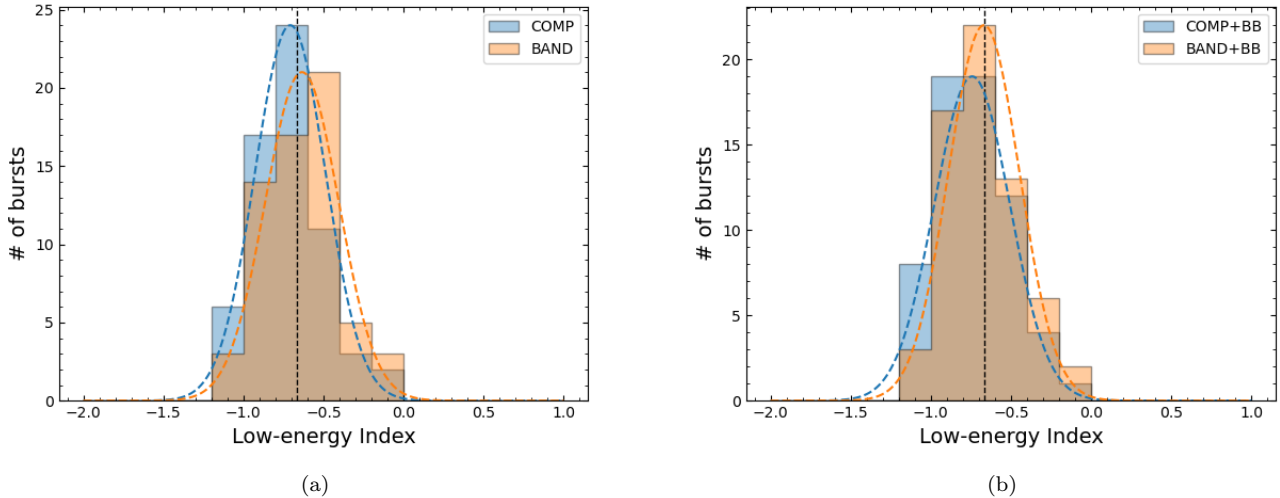


Figure 2. Distribution of the low-energy indices from COMP, BAND, COMP+BB and BAND+BB fits for long GRBs (Peak-flux Spectra). Gaussian functions showing the central value and standard deviation of the distributions are overlapped to the histograms (colour-coded dashed curves). The black dashed-line represents the synchrotron “line-of-death” value of -2/3.

- *Thermal Synchrotron*: For this model, we assume an electron distribution that consists of electrons in a thermal pool, given by

$$n_e(\gamma) = n_0 \left[\left(\frac{\gamma}{\gamma_{th}} \right)^2 \exp \left(-\frac{\gamma}{\gamma_{th}} \right) \right] \quad (7)$$

Here n_0 normalizes the distribution to total number or energy, γ is the electron Lorentz factor in the fluid frame and γ_{th} is the thermal electron Lorentz factor. We convolve this simplified distribution with the standard isotropic synchrotron kernel (Rybicki & Lightman 1979)

$$F_v(\varepsilon) \propto \int_1^\infty n_e(\gamma) \mathcal{F}\left(\frac{\varepsilon}{\varepsilon_c}\right) d\gamma, \quad (8)$$

where

$$\mathcal{F}(w) = \int_w^\infty K_{5/3}(x) dx \quad (9)$$

expresses the single-particle synchrotron emissivity (i.e., energy per unit time per unit volume) in dimensionless functional form.

2.3. PGSTAT and BIC

In previous works we have used a variant of the Cash-statistic likelihood (Cash 1979), called C-Stat in RMfit and pstat in Xspec (Arnaud et al. 2011), which assumes the background model uncertainty to be negligible. For this work, we have chosen to use pgstat, which correctly accounts for the Gaussian uncertainties in the temporally-interpolated background model, while retaining the Poisson statistics of the source counts.

We then adopt the Bayesian information criterion (BIC) to compare the fits obtained and choose the best one. The BIC is a well-known general approach to model selection that favors more parsimonious models over more complex models, i.e. it adds a penalty based on the number of parameters being estimated in the model. One form for calculating the BIC is given by:

$$BIC = -2 \ln(\hat{L}) + k \ln(n) \quad (10)$$

where \hat{L} is the maximized value of the likelihood function of the model M_k , k is the number of free parameters in the model and n is the number of data points. The model with the lowest BIC is considered the best. We can also

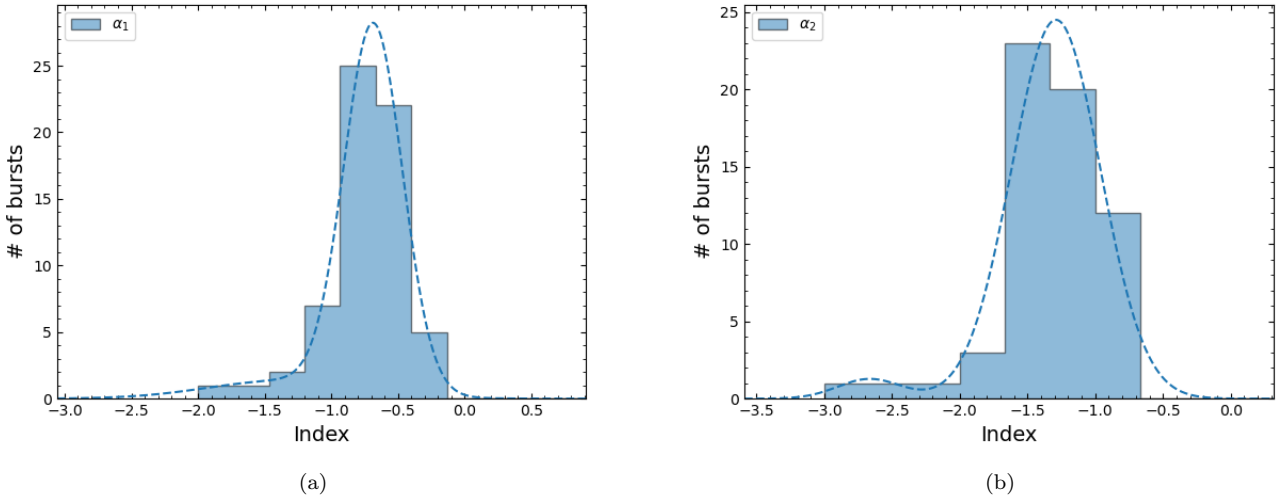


Figure 3. Distribution of the two low-energy indices from the SBPL+MBPL fits for long GRBs (Peak-flux Spectra). Gaussian functions showing the central value and standard deviation of the distributions are overlapped to the histograms (dashed curves).

calculate the Δ BIC; the difference between a particular model and the ‘best’ model with the lowest BIC, and use it as an argument against the other model. Applying these criteria, the number of bursts that classify as ‘best’ for each model can be seen in Table 2. We find that 73% of Short GRBs in the fluence spectra and 84% of Short GRBs in the peak-flux spectra have COMP as the preferred model. The low-energy index distributions from the empirical model fits for long GRBs are shown in Figure 2. Table 1 shows that out of the 100 GRBs used in this sample, 42 in the fluence spectra and 23 in the peak-flux spectra have one of the three physically motivated models as their preferred one. A detailed list of the BIC values for all bursts, for both the fluence and peak-flux spectra can be found in Table 4 and Table 5 respectively.

Table 1. Best GRB Models based on BIC

	Fluence Spectra	Peak-flux Spectra
Empirical Models	58	77
Physically-Motivated Models	42	23

3. PARAMETER DISTRIBUTIONS

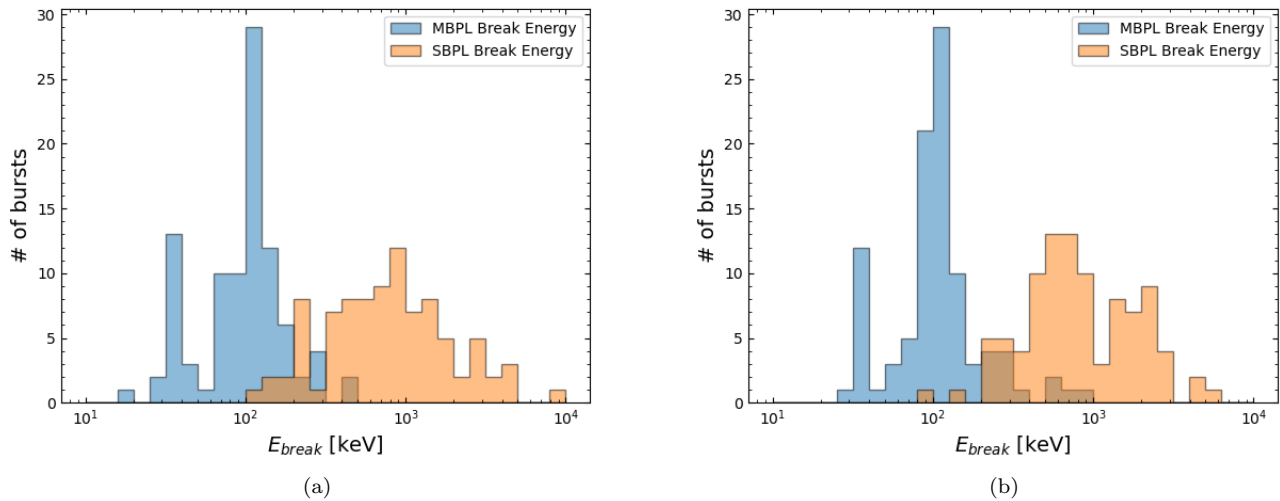
The distribution of spectral parameters help us place each burst in relation to the ensemble of all bursts. The time-integrated spectral distributions depict the overall emission properties and any spectral evolution is averaged out. For peak spectra however, the time intervals are reasonably short for any significant change of the spectral parameters.

A single electron emitting synchrotron radiation will have a spectra with slope $-2/3$ (photon index) and an exponential cutoff at high energies. The spectrum of a population of radiating electrons in the optically thin regime is just a superposition of individual spectra. For this reason the $-2/3$ value is also a hard upper limit on the overall spectral slope, also referred to as the synchrotron “line of death” (Preece et al. 1998). For a population of shock accelerated electrons, the part of the spectrum immediately below the νF_ν peak energy will display a power-law behavior with a slope $\sim -3/2$, which breaks to a harder spectral shape (slope $\sim -2/3$, following the single electron spectrum) at lower energies. This is in the so called fast-cooling regime, where random Lorentz factor of an electron that cools on the dynamic timescale, is lower than the typical injected electron’s energy (Sari et al. 1998).

Figure 2 shows the distribution of low-energy indices of long GRBs (Peak-flux spectra) from the four empirical models used in this work. They have a combined median value of $\sim -0.69^{+0.20}_{-0.22}$, aligning with the $-2/3$ expectation. The distribution of the two low-energy indices from the SBPL+MBPL fits for peak-flux spectra of long GRBs are shown

Table 2. BIC Comparison (Number of GRBs for which the given model has the lowest value of BIC)

Model	Total (fluence)	Total (peak-flux)	Long GRBs (fluence)	Short GRBs (fluence)	Long GRBs (peak-flux)	Short GRBs (peak-flux)
TS	9	2	4	5	2	0
COMP	31	41	4	27	10	31
COMP+BB	2	9	2	0	7	2
BAND	11	15	10	1	13	2
BAND+BB	14	12	14	0	11	1
BAND+H.E. Cutoff	12	14	9	3	13	1
SBPL+MBPL	21	7	20	1	7	0

**Figure 4.** Distribution of the two break energies from the fluence (a) and peak-flux (b) spectral fits for SBPL+MBPL.

in Figure 3; the two distributions have median values of $-0.72_{-0.21}^{+0.20}$ (α_1) and $-1.32_{-0.24}^{+0.33}$ (α_2) respectively (Table 3). These values are in line with the -2/3 and -3/2 expected indices for synchrotron spectrum from fast-cooling electrons. This result lends strong support for the case of synchrotron radiation as the primary emission mechanism for GRB prompt emission.

It is evident from Figure 2, 3 that a non-negligible fraction of GRBs have a low-energy index value steeper than -2/3, which presents a challenge for the synchrotron theory. One possibility in such cases would be the appearance of a quasi-thermal component of photospheric origin (Mészáros & Rees 2000; Daigne & Mochkovitch 2002). The emission from both the photosphere and internal shocks have a similar duration, the latter having only a very short lag behind the first. The intensity of the photospheric emission depends strongly on the unknown mechanism responsible for the acceleration of the relativistic outflow (Daigne et al. 2011). Another possibility to consider is the effect of electron pitch angle scattering (Lloyd & Petrosian 2000); where a small pitch angle leads to a harder low-energy index value ($-2/3 \lesssim \alpha \lesssim 0$) and a large pitch angle can accommodate bursts below the “line of death” ($\alpha \lesssim -2/3$). Spectral indices harder than -3/2 can be obtained by more elaborate models. For example, Derishev (2007); Zhao et al. (2014) showed that fast cooling electrons in decaying magnetic fields can lead to such hard spectra.

Figure 4 shows the distribution of the two break energies from the SBPL+MBPL model. Interestingly, we find a subgroup of GRBs that have a low-energy break between 30-40 keV in both the fluence and peak-flux spectral fits. A similar low-energy break was found in GRB 221009A (Lesage et al. 2023) and will be investigated further in a future

Table 3. The median parameter values and the 68% CL for all long and short GRBs

Model	Long GRBs			Short GRBs		
	L.E. Index	H.E. Index	E_{peak} (keV)	L.E. Index	H.E. Index	E_{peak} (keV)
Fluence Spectra						
COMP	$-0.97^{+0.20}_{-0.20}$...	372^{+412}_{-162}	$-0.58^{+0.28}_{-0.30}$...	1024^{+331}_{-512}
COMP+BB	$-0.99^{+0.21}_{-0.21}$...	434^{+477}_{-183}	$-0.65^{+0.24}_{-0.23}$...	982^{+516}_{-477}
BAND	$-0.91^{+0.19}_{-0.18}$	$-2.41^{+0.23}_{-0.39}$	308^{+473}_{-143}	$-0.54^{+0.26}_{-0.27}$	$-3.28^{+1.09}_{-7.93}$	967^{+371}_{-516}
BAND+BB	$-0.93^{+0.27}_{-0.19}$	$-2.55^{+0.32}_{-0.80}$	378^{+486}_{-226}	$-0.55^{+0.19}_{-0.27}$	$-3.18^{+1.05}_{-5.21}$	903^{+471}_{-482}
SBPL+MBPL	$-0.97^{+0.23}_{-0.30}, -1.41^{+0.27}_{-0.48}$	$-2.61^{+0.44}_{-0.46}$	497^{+470}_{-290}	$-0.59^{+0.35}_{-0.32}, -0.94^{+0.24}_{-0.45}$	$-3.15^{+0.91}_{-3.59}$	1074^{+584}_{-496}
Peak Flux Spectra						
COMP	$-0.71^{+0.20}_{-0.19}$...	423^{+803}_{-164}	$-0.27^{+0.29}_{-0.36}$...	830^{+509}_{-318}
COMP+BB	$-0.74^{+0.24}_{-0.22}$...	468^{+739}_{-132}	$-0.46^{+0.37}_{-0.27}$...	857^{+606}_{-300}
BAND	$-0.60^{+0.14}_{-0.22}$	$-2.66^{+0.40}_{-1.06}$	377^{+770}_{-161}	$-0.22^{+0.37}_{-0.39}$	$-4.80^{+2.41}_{-6.06}$	834^{+500}_{-385}
BAND+BB	$-0.68^{+0.22}_{-0.20}$	$-2.91^{+0.53}_{-1.11}$	468^{+471}_{-199}	$-0.39^{+0.61}_{-0.37}$	$-4.58^{+2.13}_{-4.70}$	895^{+519}_{-406}
SBPL+MBPL	$-0.72^{+0.20}_{-0.21}, -1.32^{+0.33}_{-0.24}$	$-3.11^{+0.67}_{-1.34}$	493^{+694}_{-162}	$-0.30^{+0.62}_{-0.36}, -0.89^{+0.45}_{-0.28}$	$-4.30^{+1.59}_{-5.90}$	905^{+533}_{-342}

work. In the scenario where a low-energy spectral break is a common feature in GRB spectra, it has been suggested that the average low-energy spectral index value of $\alpha \sim -1$ (Gruber et al. 2014; Poolakkil et al. 2021) is an average value between the two power-law segments below and above the break energy (Toffano et al. 2021). We find that for our sample of bursts, only long GRBs from the peak-flux spectra satisfy this condition (Table 3).

4. SUMMARY

The goal of this work is to explore the use of physically-motivated models to fit GRB spectra and directly compare them to the empirical models used in previous GBM spectroscopy catalogs (Goldstein et al. 2012; Gruber et al. 2014). The spectral properties presented here are from time-integrated and peak flux analysis, produced using seven photon models; four empirical and three physically-motivated. We use a sample of 100 GRBs, that were selected based on their energy flux values (Poolakkil et al. 2021). We have used pgstat as our fitting statistic; which accounts for the Gaussian uncertainties in the background model, while retaining the Poisson statistics of the source counts, and then use the Bayesian information criterion (BIC) to compare fits and choose the best model.

We found that 42% of the GRBs from the fluence spectra and 23% of GRBs from the peak-flux spectra had one of the three physically-motivated models as their preferred one. The low-energy index distributions from the empirical model fits for long GRBs (peak-flux spectra), highlighted in Figure 2, peak around the synchrotron value of $-2/3$, while the two low-energy indices from the SBPL+MBPL fits of long GRBs (peak-flux spectra, Figure 3) peak close to the $-2/3$ and $-3/2$ values expected for synchrotron spectrum below and above the cooling frequency. These results present a strong case for synchrotron radiation as a leading mechanism for the origin of prompt emission from GRBs and further encourage the transition from empirical models towards physically-motivated models to fit GRB spectra.

The UAH co-authors gratefully acknowledge NASA funding from co-operative agreement 80MSFC22M0004.

Table 4. BIC Comparison (Fluence Spectra). The best model is indicated with an *

ID	TS	COMP	COMP+BB	BAND	BAND+BB	BAND+H.E.C	SBPL+MBPL
Short GRBs							
GRB 170305256	520.29	502.81*	514.29	512.22	523.76	503.21	524.21
GRB 100223110	402.04	343.67*	353.61	349.59	359.48	366.13	357.25

Table 4 continued on next page

Table 4 (*continued*)

ID	TS	COMP	COMP+BB	BAND	BAND+BB	BAND+H.E.C	SBPL+MBPL
GRB 120817168	551.69	549.77*	562.02	555.96	568.16	553.63	566.14
GRB 110529034	458.97*	468.32	480.98	470.75	483.07	469.75	483.5
GRB 180402406	582.6	531.31*	531.52	537.72	546.1	543.79	537.54
GRB 120624309	558.15	523.56	523.51	529.21	527.84	598.61	523.36*
GRB 130701761	533.26	432.26*	434.34	438.36	440.44	438.35	445.76
GRB 170219002	231.8*	238.44	244.87	244.28	255.49	236.75	250.86
GRB 140209313	535.41	442.16	423.7	412.69	413.99	408.59*	446.9
GRB 090227772	836.32	545.88*	552.22	549.3	555.26	582.4	548.49
GRB 170816599	568.19	501.91*	510.62	508.09	516.81	503.97	517.1
GRB 170708046	490.4*	503.12	505.58	501.34	513.16	492.82	512.75
GRB 130804023	518.35	515.33*	527.55	521.25	532.61	515.38	533.82
GRB 130628860	493.79	487.86	499.97	494.07	506.13	487.79*	506.11
GRB 100811108	627.64	504.62*	513.52	511.31	520.4	551.91	520.72
GRB 091012783	413.61	384.0*	395.3	389.87	401.61	387.56	400.66
GRB 180204109	510.18*	514.89	526.55	521.87	533.69	518.83	534.71
GRB 090510016	487.08	484.15*	493.15	486.64	492.85	504.56	494.15
GRB 110705151	629.85	483.33*	483.68	490.84	491.16	533.44	495.08
GRB 170127067	607.27	238.33*	248.93	242.76	253.78	379.68	249.58
GRB 121127914	410.24	397.18*	408.26	403.11	492.63	397.34	412.5
GRB 150922234	522.61	514.68*	525.04	520.77	532.42	515.08	532.05
GRB 140901821	790.89	551.71*	556.49	557.96	562.67	604.92	568.96
GRB 111222619	523.8	397.59*	409.44	403.48	415.12	413.62	415.21
GRB 161218222	553.44	503.42*	515.4	509.44	521.57	515.72	518.04
GRB 150819440	480.21	444.13*	447.56	450.04	453.44	512.65	456.33
GRB 150811849	502.21	377.0*	386.21	382.58	392.16	409.67	395.1
GRB 130515056	390.97	375.3*	385.82	381.47	392.74	379.17	393.3
GRB 100206563	563.52	554.07*	566.35	558.68	568.43	557.63	568.93
GRB 131126163	421.71	370.5	379.11	369.03*	380.78	392.54	381.77
GRB 180703949	762.43	572.08	574.34	573.96	580.27	569.56*	650.02
GRB 081216531	557.73	555.17*	567.51	560.93	566.42	555.48	560.26
GRB 081209981	354.35	349.15*	359.72	356.22	366.87	350.51	367.4
GRB 141011282	489.65	482.31*	494.52	488.46	500.68	482.39	500.72
GRB 150118927	531.28*	543.08	549.77	546.12	553.75	536.66	556.97
GRB 120811014	456.22	381.04*	391.21	386.93	397.09	402.99	399.36
GRB 090617208	495.44	485.2*	497.15	492.19	504.32	489.95	504.1
Long GRBs							
GRB 090424592	943.46	904.7	908.36	896.75*	902.77	974.74	907.22
GRB 160802259	526.33	396.64	346.75	375.57	352.17	325.22*	359.68
GRB 160422499	965.24*	1088.0	997.55	1018.5	1002.31	1109.41	988.35
GRB 131028076	980.67	595.22	591.52	590.07	597.68	612.87	583.79*
GRB 131014215	6203.19	1389.08	1059.02	1130.08	1028.82*	1494.34	1042.63
GRB 081009140	683.84	675.21*	687.56	677.42	689.84	2876.54	945.1
GRB 140206275	3086.79	1785.7	1697.75	1732.73	1678.66*	1833.17	1696.65
GRB 140329295	845.54	1009.1	793.84	810.49	724.86	701.44	692.03*
GRB 180218635	465.24	375.01	345.46	318.97	311.01*	317.28	313.66
GRB 110921912	523.83*	567.53	554.52	562.72	556.55	550.56	560.53
GRB 130606497	3282.79	2573.84	2327.23	2166.65	2048.68*	2345.2	2199.81

Table 4 continued on next page

Table 4 (*continued*)

ID	TS	COMP	COMP+BB	BAND	BAND+BB	BAND+H.E.C	SBPL+MBPL
GRB 150201574	1215.08	1179.7	1103.17	1098.89	1087.78*	1127.39	1359.07
GRB 150118409	1000.63	826.55*	829.55	831.46	834.55	1428.47	840.13
GRB 090618353	2268.14	2417.27	2299.55	2183.23*	2194.57	2300.75	2240.15
GRB 171010792	6546.13	8247.58	6841.33	6932.89	5208.78	5626.73	5030.72*
GRB 180113418	2136.99	2424.76	1607.83	1743.1	1457.65	1535.91	1317.56*
GRB 150902733	1619.4	945.88	772.38	808.85	743.54*	840.72	754.96
GRB 180113011	697.05	691.22*	703.06	694.66	706.03	744.81	704.02
GRB 100701490	512.2	523.73	527.83	501.63*	509.23	535.97	511.47
GRB 170409112	1432.47	1462.62	1304.64	1365.75	1326.63	1752.57	1256.37*
GRB 120426090	772.78	526.49	500.81	516.3	505.27	493.39*	499.03
GRB 140508128	585.67	548.09	558.34	529.48*	530.49	600.19	554.45
GRB 150330828	1703.4	1804.39	1702.53	1643.69*	1657.5	1809.89	1657.99
GRB 100719989	811.92	769.56	738.87	734.26	732.43	720.68*	734.11
GRB 131229277	635.12	511.93*	519.3	518.0	522.26	526.88	520.86
GRB 180305393	1361.37	773.62	722.06	734.21	721.81*	793.52	722.52
GRB 170115743	1702.69*	1725.64	1708.17	1722.08	1713.56	1731.59	1724.21
GRB 170527480	1475.9	947.69	906.9	953.82	913.11	1659.17	891.5*
GRB 110825102	840.33	806.61	795.5	804.54	800.68	958.97	795.27*
GRB 130502327	1797.47	1108.26	1120.67	1046.05*	1055.15	1059.01	1058.96
GRB 101014175	2518.6	2454.94	2325.33	2211.06	2222.85	2469.62	2208.61*
GRB 150510139	1108.36	734.44	705.58*	740.59	711.72	1437.97	710.12
GRB 161218356	3091.88	951.0	938.05	920.17*	930.9	951.09	949.41
GRB 120129580	576.46	501.91	435.06	484.29	431.59	437.62	419.8*
GRB 110625881	1378.57	1330.78	1262.54	1232.64	1171.76*	1236.37	1255.76
GRB 100826957	1976.3	2401.01	2098.61	1881.26	1675.54	1839.42	1669.4*
GRB 130305486	859.9	823.28	835.61	818.15	830.55	804.69*	819.51
GRB 170808936	1270.6	1247.67	1164.34	1171.63	1157.08	1509.21	1131.69*
GRB 160625945	4789.32	4819.52	4194.59	4414.85	4032.48	5500.55	4023.77*
GRB 090926181	4999.25	4640.18	4570.88	4581.35	4525.12	8281.4	4513.64*
GRB 140416060	384.73*	444.95	393.13	408.23	408.19	431.21	482.19
GRB 110301214	1193.92	1090.62	1009.64	1001.04	958.07*	965.81	1291.02
GRB 151231443	647.94	678.06	639.99	609.65	590.24	607.29	577.96*
GRB 130518580	1198.89	1208.92	1193.74	1177.23	1156.13*	1230.43	1158.63
GRB 091003191	635.59	626.53	636.14	623.81*	635.59	676.12	637.77
GRB 150403913	990.77	1078.27	996.93	1026.15	982.3	994.78	979.18*
GRB 090820027	2197.92	998.4	863.67	878.55	860.08	828.7*	856.26
GRB 090902462	4282.2	2398.21	1676.52	2404.35	1682.67	6148.28	1498.67*
GRB 171119992	323.57	334.03	345.01	328.48	335.33	321.69*	334.31
GRB 160910722	1014.37	1070.07	974.77	970.76	955.21	953.62	952.05*
GRB 120711115	1166.6	1023.68	1035.34	982.27*	986.11	1506.99	987.48
GRB 100829876	397.55	416.83	403.81	401.25	408.6	392.9*	408.59
GRB 150213001	1027.48	1187.29	1076.79	1066.79	972.23*	1430.02	1313.7
GRB 101123952	1097.33	1203.98	1175.41	1109.9	1082.61	1177.54	1076.64*
GRB 081215784	797.17	833.56	773.92	763.74	739.82	724.31*	748.55
GRB 131231198	2387.55	2229.76	2124.67	2088.08	2020.39*	2131.04	2136.43
GRB 160720767	1204.47	1195.51	1173.47*	1183.06	1176.26	1300.46	1189.69
GRB 150627183	1295.11	1522.15	1414.78	1327.61	1289.08*	1482.12	1394.34

Table 4 *continued on next page*

Table 4 (*continued*)

ID	TS	COMP	COMP+BB	BAND	BAND+BB	BAND+H.E.C	SBPL+MBPL
GRB 160530667	2133.07	1109.48	986.9	952.01	940.4	916.17*	1042.49
GRB 140102887	671.8	605.1	614.73	601.09*	610.02	625.96	662.68
GRB 160509374	1347.4	1383.35	1396.4	1309.6	1321.38	1633.8	1300.26*
GRB 160821857	4327.84	2844.16	2650.69	2429.59	2335.56*	4864.24	2362.25
GRB 150210935	755.17	566.09	538.64	572.27	544.77	849.58	535.46*

Table 5. BIC Comparison (Peak-flux Spectra). The best model is indicated with an *

ID	TS	COMP	COMP+BB	BAND	BAND+BB	BAND+H.E.C	SBPL+MBPL
Short GRBs							
GRB 170305256	501.08	470.17*	476.24	480.2	485.45	480.53	492.58
GRB 100223110	410.17	319.05*	340.22	324.91	335.87	373.48	333.53
GRB 120817168	546.63	535.22*	547.73	541.82	548.18	535.3	548.84
GRB 110529034	495.51	491.57*	494.07	498.41	500.9	505.29	500.84
GRB 180402406	561.08	530.84*	543.17	538.32	549.31	546.18	546.13
GRB 120624309	615.61	582.02	573.65*	588.35	580.42	583.49	580.7
GRB 130701761	469.61	454.73*	461.21	460.83	467.3	461.13	467.1
GRB 170219002	214.25	207.95*	218.32	213.79	224.03	236.75	223.64
GRB 140209313	461.14	391.15	380.19*	382.94	384.87	395.59	384.92
GRB 090227772	1194.71	510.8	516.37	507.09*	515.1	878.5	514.75
GRB 170816599	579.56	481.08*	491.56	487.37	497.94	530.51	498.09
GRB 170708046	484.0	490.02	482.41	475.69*	487.86	479.13	486.31
GRB 130804023	648.78	568.4*	577.7	653.97	605.72	596.1	586.25
GRB 130628860	541.73	508.59	519.32	514.71	506.08*	520.96	506.11
GRB 100811108	585.16	539.34*	548.02	546.25	554.59	564.0	551.46
GRB 091012783	350.11	329.4*	340.96	335.51	346.92	335.91	345.85
GRB 180204109	505.56	483.92*	495.29	490.29	502.63	488.38	501.56
GRB 090510016	460.4	442.46*	452.11	449.07	458.43	442.84	460.25
GRB 110705151	571.1	484.53*	492.66	491.47	499.64	519.72	501.19
GRB 170127067	520.46	248.25*	253.89	253.75	266.19	369.71	260.91
GRB 121127914	353.51	339.71*	408.25	403.11	349.61	343.99	355.88
GRB 150922234	493.62	461.22*	472.98	467.42	479.16	472.89	478.11
GRB 140901821	554.9	497.2*	508.81	503.37	514.99	510.45	514.46
GRB 111222619	424.32	414.79*	426.39	421.51	431.56	415.14	431.17
GRB 161218222	548.71	531.44*	543.12	537.62	549.38	536.9	546.84
GRB 150819440	733.35	402.54*	406.27	408.43	405.89	538.07	403.79
GRB 150811849	384.15	376.43*	382.79	382.36	388.68	377.49	392.1
GRB 130515056	377.85	363.33*	374.88	369.14	380.42	370.07	379.39
GRB 100206563	559.86	545.32*	553.89	550.05	560.42	551.82	558.53
GRB 131126163	376.45	333.25*	343.46	336.31	347.49	361.01	347.56
GRB 180703949	551.25	423.08*	433.2	429.22	439.47	430.14	439.5
GRB 081216531	563.22	518.73*	530.56	525.44	537.05	529.24	533.2
GRB 081209981	357.69	333.92*	343.64	340.9	354.62	342.87	352.79
GRB 141011282	484.6	479.28*	490.72	484.48	495.66	480.09	495.34
GRB 150118927	474.76	467.64	475.96	470.61	482.3	466.16*	481.65

Table 5 *continued on next page*

Table 5 (*continued*)

ID	TS	COMP	COMP+BB	BAND	BAND+BB	BAND+H.E.C	SBPL+MBPL
GRB 120811014	406.14	332.68*	342.88	338.58	348.81	380.51	348.26
GRB 090617208	528.9	482.82*	494.72	489.34	501.63	516.92	501.41
Long GRBs							
GRB 090424592	731.5	590.27	590.83	589.6*	592.11	591.88	591.29
GRB 160802259	874.02	299.84	286.36	291.11	283.24*	388.32	284.19
GRB 160422499	674.42	647.3	588.9	625.6	592.38	575.86*	596.75
GRB 131028076	1241.96	418.56	427.21	410.92*	421.55	498.67	418.31
GRB 131014215	9618.96	1085.59	698.91	751.05	615.14	4140.4	605.23*
GRB 081009140	705.99	400.86	400.32*	406.76	405.21	423.72	568.6
GRB 140206275	674.78	555.27	557.03	527.21*	538.55	531.38	538.38
GRB 140329295	605.67	594.26	510.29	490.02	470.81*	475.17	476.88
GRB 180218635	527.76	324.26	322.86	308.71	307.7	322.23	302.71*
GRB 110921912	463.93	449.24	437.97	439.69	437.13	428.84*	437.77
GRB 130606497	692.45	712.17	666.94	632.2	631.58	656.47	616.49*
GRB 150201574	973.97	705.73	665.83	642.42*	654.79	654.8	700.8
GRB 150118409	661.54	530.08*	540.87	536.25	547.04	537.92	551.03
GRB 090618353	318.0*	335.95	326.0	336.35	330.72	318.35	331.09
GRB 171010792	468.69	492.1	458.17	458.18	437.43	424.27*	428.96
GRB 180113418	708.69	707.96	648.21	626.3	594.54*	624.1	603.89
GRB 150902733	1152.88	559.62	526.73	531.24	509.28*	610.55	518.25
GRB 180113011	677.4	524.13*	532.24	529.99	537.92	525.92	540.14
GRB 100701490	493.77	413.46	415.08	395.24*	403.74	403.78	405.86
GRB 170409112	1157.08	634.07	592.73	619.0	592.33*	611.1	600.44
GRB 120426090	880.13	453.93	436.61*	457.04	441.89	454.14	438.1
GRB 140508128	391.64	325.25	327.41	287.21*	297.07	299.83	295.34
GRB 150330828	581.82	603.66	592.92	571.91*	583.66	578.2	579.5
GRB 100719989	660.88	475.24	462.51	460.84	459.19	465.95	455.99*
GRB 131229277	983.59	484.71*	496.63	486.5	498.7	655.4	495.23
GRB 180305393	781.32	578.83	567.97*	579.81	576.1	594.92	584.07
GRB 170115743	896.02	668.38*	678.22	674.58	1119.1	693.15	683.0
GRB 170527480	759.86	531.84	522.87*	538.27	529.13	544.0	526.8
GRB 110825102	633.42	529.06*	532.76	535.24	535.8	533.92	532.0
GRB 130502327	1264.4	572.84*	584.27	576.73	586.78	682.54	583.45
GRB 101014175	370.37*	442.97	405.19	401.23	385.78	372.24	389.59
GRB 150510139	772.32	505.92*	506.7	512.07	512.9	506.57	514.07
GRB 161218356	959.21	566.44	559.43	560.0	557.42*	567.05	577.48
GRB 120129580	833.77	397.36	338.73	351.32	328.74*	359.51	336.76
GRB 110625881	770.2	645.13	560.86	571.06	561.42	550.44*	582.45
GRB 100826957	443.94	466.43	446.02	435.02	432.24	424.87*	427.15
GRB 130305486	761.15	536.88	534.46	529.88*	537.22	561.81	537.21
GRB 170808936	741.55	732.2	678.21	680.3	664.47	638.2*	684.86
GRB 160625945	1909.5	2699.83	1473.65	1256.17	1038.53	1331.1	824.75*
GRB 090926181	1225.21	602.96	575.16	590.93	574.46*	611.98	579.78
GRB 140416060	286.58	281.57*	292.12	287.07	296.17	286.43	301.18
GRB 110301214	767.22	708.29	680.4	674.25	660.69	657.64*	664.03
GRB 151231443	380.89	379.98	380.22	379.26	376.28	365.65*	377.56
GRB 130518580	597.18	640.17	599.56	600.77	602.83	576.77*	602.13

Table 5 *continued on next page*

Table 5 (*continued*)

ID	TS	COMP	COMP+BB	BAND	BAND+BB	BAND+H.E.C	SBPL+MBPL
GRB 091003191	455.9	405.36	417.14	397.04	403.89	390.66*	402.89
GRB 150403913	458.33	478.33	478.51	442.39	443.45	431.85*	439.45
GRB 090820027	1079.08	539.73	493.36*	507.85	497.72	502.53	501.37
GRB 090902462	2585.62	1548.01	706.96	1554.2	712.99	3098.02	548.12*
GRB 171119992	290.5	287.47	297.42	290.51	299.02	284.21*	298.19
GRB 160910722	1816.26	729.31	650.27	557.52	548.95*	880.89	561.04
GRB 120711115	394.08	415.27	425.09	393.79*	403.29	405.85	404.28
GRB 100829876	373.09	307.73	282.73*	292.48	288.57	294.39	292.43
GRB 150213001	866.19	783.68	756.91	732.69	725.53*	748.31	886.65
GRB 101123952	485.33	437.88*	447.96	443.78	453.85	442.85	451.86
GRB 081215784	906.74	751.13	704.97	566.27*	575.45	630.0	566.94
GRB 131231198	716.52	609.54	622.07	596.42*	607.78	615.48	603.89
GRB 160720767	521.93	459.06*	463.72	463.33	469.32	462.4	471.41
GRB 150627183	510.46	479.38	469.48	460.21	468.68	451.13*	473.14
GRB 160530667	1341.14	732.46	664.92	652.24	650.94	663.68	642.24*
GRB 140102887	819.08	554.27	548.88	527.02*	536.78	536.6	718.96
GRB 160509374	674.09	666.91	659.04	604.77*	616.18	613.71	615.55
GRB 160821857	724.48	905.87	803.15	620.44	596.31*	718.81	610.33
GRB 150210935	849.99	595.01	576.19*	599.31	580.34	582.13	586.18

REFERENCES

- Arnaud, K., Smith, R., & Siemiginowska, A. 2011, Handbook of X-ray Astronomy (Cambridge University Press)
- Arnold, B. C. 2015, 1, doi: <https://doi.org/10.1002/9781118445112.stat01100.pub2>
- Band, D., Matteson, J., Ford, L., et al. 1993, ApJ, 413, 281, doi: [10.1086/172995](https://doi.org/10.1086/172995)
- Bauke, H. 2007, European Physical Journal B, 58, 167, doi: [10.1140/epjb/e2007-00219-y](https://doi.org/10.1140/epjb/e2007-00219-y)
- Cash, W. 1979, ApJ, 228, 939, doi: [10.1086/156922](https://doi.org/10.1086/156922)
- Daigne, F., Bošnjak, Ž., & Dubus, G. 2011, A&A, 526, A110, doi: [10.1051/0004-6361/201015457](https://doi.org/10.1051/0004-6361/201015457)
- Daigne, F., & Mochkovitch, R. 2002, MNRAS, 336, 1271, doi: [10.1046/j.1365-8711.2002.05875.x](https://doi.org/10.1046/j.1365-8711.2002.05875.x)
- Derishev, E. V. 2007, Ap&SS, 309, 157, doi: [10.1007/s10509-007-9421-z](https://doi.org/10.1007/s10509-007-9421-z)
- Goldstein, A., Burgess, J. M., Preece, R. D., et al. 2012, ApJS, 199, 19, doi: [10.1088/0067-0049/199/1/19](https://doi.org/10.1088/0067-0049/199/1/19)
- Gruber, D., Goldstein, A., Weller von Ahlefeld, V., et al. 2014, ApJS, 211, 12, doi: [10.1088/0067-0049/211/1/12](https://doi.org/10.1088/0067-0049/211/1/12)
- Katz, J. I. 1994, ApJL, 432, L107, doi: [10.1086/187523](https://doi.org/10.1086/187523)
- Kouveliotou, C., Meegan, C. A., Fishman, G. J., et al. 1993, ApJL, 413, 101, doi: [10.1086/186969](https://doi.org/10.1086/186969)
- Lesage, S., Veres, P., Briggs, M. S., et al. 2023, arXiv e-prints, arXiv:2303.14172, doi: [10.48550/arXiv.2303.14172](https://doi.org/10.48550/arXiv.2303.14172)
- Lloyd, N. M., & Petrosian, V. 2000, ApJ, 543, 722, doi: [10.1086/317125](https://doi.org/10.1086/317125)
- Meegan, C., Lichti, G., Bhat, P. N., et al. 2009, ApJ, 702, 791, doi: [10.1088/0004-637X/702/1/791](https://doi.org/10.1088/0004-637X/702/1/791)
- Mészáros, P., & Rees, M. J. 2000, ApJ, 530, 292, doi: [10.1086/308371](https://doi.org/10.1086/308371)
- Neath, A. A., & Cavanaugh, J. E. 2012, WIREs Computational Statistics, 4, 199, doi: <https://doi.org/10.1002/wics.199>
- Oganesyan, G., Nava, L., Ghirlanda, G., & Celotti, A. 2017, ApJ, 846, 137, doi: [10.3847/1538-4357/aa831e](https://doi.org/10.3847/1538-4357/aa831e)
- Poolakkil, S., Preece, R., Fletcher, C., et al. 2021, ApJ, 913, 60, doi: [10.3847/1538-4357/abf24d](https://doi.org/10.3847/1538-4357/abf24d)
- Preece, R. D., Briggs, M. S., Mallozzi, R. S., et al. 1998, ApJ, 505, L23, doi: [10.1086/311644](https://doi.org/10.1086/311644)
- Ravasio, M. E., Ghirlanda, G., Nava, L., & Ghisellini, G. 2019, A&A, 625, A60, doi: [10.1051/0004-6361/201834987](https://doi.org/10.1051/0004-6361/201834987)
- Rees, M. J., & Meszaros, P. 1994, ApJL, 430, L93, doi: [10.1086/187446](https://doi.org/10.1086/187446)
- Rybicki, G. B., & Lightman, A. P. 1979, Radiative Processes in Astrophysics (Wiley-VCH)

- Sari, R., Piran, T., & Narayan, R. 1998, ApJL, 497, L17,
doi: [10.1086/311269](https://doi.org/10.1086/311269)
- Tavani, M. 1996, ApJ, 466, 768, doi: [10.1086/177551](https://doi.org/10.1086/177551)
- Toffano, M., Ghirlanda, G., Nava, L., et al. 2021, A&A,
652, A123, doi: [10.1051/0004-6361/202141032](https://doi.org/10.1051/0004-6361/202141032)
- Zhao, X., Li, Z., Liu, X., et al. 2014, ApJ, 780, 12,
doi: [10.1088/0004-637X/780/1/12](https://doi.org/10.1088/0004-637X/780/1/12)